Deformable Model of the Heart With Fiber Structure

Arkadiusz Sitek, *Member, IEEE*, Gregory J. Klein, *Member, IEEE*, Grant T. Gullberg, *Senior Member, IEEE*, and Ronald H. Huesman, *Fellow, IEEE*

***Abstract*—A kinematic model of the heart with incompressibility constraints was implemented. It accounts for the effects of the heart fiber structure, which plays a major role in defining the exact motion of the heart during the cardiac cycle. The volume of the heart was divided into small hexahedral elements, and in each element the fiber direction was specified. This allows implementation of nearly any fiber structure and any geometry. We performed preliminary tests on the model. The model was deformed from its initial state to a final configuration. It was assumed that the fibers shorten or elongate to some known new value for each element. This, along with incompressibility constraints, could simulate a beating heart if the elongations of the fibers are known. The model was also deformed using imaging data as *a priori* information. Simple geometries of the cylinder and ellipsoid were investigated. The model can be used as a tool to help in understanding the movement of the myocardium during the heart cycle, and the impact of infarctions on that movement.**

***Index Terms*—Deformable models, SPECT.**

I. Introduction

KNOWLEDGE of the heart's movement during the cardiac cycle is an important indication of heart performance and health. Imaging methods such as gated SPECT and PET, or cine MRI, can be used to measure heart movement. These methods, especially gated SPECT and PET, give limited results due to poor resolution and noise. Useful diagnostic features of this movement, such as twisting of the heart muscle or thickening, are difficult or even sometimes impossible to measure using SPECT or PET techniques. In this paper, we present a deformable model that can be used to estimate heart movement. Using this model, values of the left ventricle ejection fraction (LVEF) and myocardial wall thickening can be estimated more precisely than with direct estimation from gated nuclear medicine studies.

In order to parameterize cardiac contractile motion seen in images from gated studies, the images of different time gates can be warped with elastic constraints to match each other [1]. However, these elastic constraints do not take into account fiber structure of the heart muscle. Because of that, the motion field found by this method may not be accurate.

Manuscript received August 2000; revised August 2001.

A. Sitek was with the University of Utah, Salt Lake City, UT 84132 USA. He is now with the Beth Israel Medical Center, Boston, MA 02215 USA (e-mail: asitek@caregroup.harvard.edu).

G. J. Klein and R. H. Huesman are with the Center for Functional Imaging, E.O. Lawrence Berkeley National Laboratory, Berkeley, CA 94720 USA (e-mail: gjklein@lbl.gov; rhhuesman@lbl.gov).

G. T. Gullberg was with the Radiology Department, University of Utah, Salt Lake City, UT 84132 USA. He is now with the Center for Advanced Imaging, E. O. Lawrence Berkeley National Laboratory, Berkeley, CA 94720 USA.

Publisher Item Identifier S 0018-9499(02)06186-5.

One approach to determining more accurate heart movement would be to use finite-element methods [2]–[5]. In this approach, the heart configuration during the heart cycle is calculated using the balance of forces between the stresses in the heart muscle and intraventricular pressure. Imaging data can be used in this approach as *a priori* information [3]. The disadvantage of using finite-element methods is that the material parameters must be known in order to determine the balance of forces. It has been shown [6] that the material parameters depend on the strain, state of activation, time after activation, and location in the heart muscle. All of these factors make the simulation of a beating heart with finite-element methods extremely difficult.

In this paper, we describe a deformable parametric model of the heart. In this model, we use the same meshes as used in finite-element methods. The balance of forces, however, is not calculated, so the specification of extremely complicated material constraints is not necessary. The only regularization constraint used during deformation of the model is incompressibility. The deformation can be driven either by specification of the fiber shortening/elongation for each element, or by imaging information. We present results of computer simulations of the model for some simple geometries of the cylinder and ellipsoid.

II. Methods

The kinematics of the model will be presented in Section II-A. In Section II-B, the implementation of imaging data as a driving force of the deformation will be presented.

A. Deformable Model and Computer Implementation

The volume of the heart muscle is approximated by a set of points, called *nodes*, located at specific places in the heart muscle. These points are attached to the object and change position when the object is deforming. Nodes define hexahedral regions (Fig. 1) which will be called *elements*. The geometry over each element are approximated using values for eight nodes, which define any particular element. The geometry of each element is interpolated from the nodes as follows:

$$\boldsymbol{X} = \sum_{a=1}^{8} N_a(\xi_1, \xi_2, \xi_3)\boldsymbol{X}_a \tag{1}$$

where $\boldsymbol{X}$ is the coordinate vector in the initial configuration, N_a is the trilinear approximation function, and $\boldsymbol{X}_a$ is the coordinate of a node a in the initial configuration. ξ_1, ξ_2, and ξ_3 are the coordinates of a point inside the element, which is being approximated in the local coordinate system of an element [see Fig. 1(a)]. Each element has its own independent local

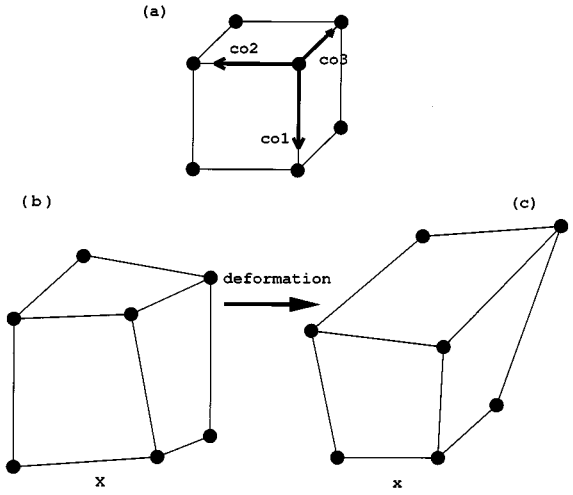

Fig. 1. Schematic representation of one element with black dots representing the nodes. (a) Element (perfect cube) in local coordinate system. (b) Initial configuration ($\boldsymbol{X}$) of an element. (c) A deformed configuration of that element. The deformation from (b) to (c) is described by the deformation gradient $\hat{\boldsymbol{F}}$.

coordinate system. For more information on the interpolation functions please refer to [4]. The same interpolation is used for the deformed configuration

$$\boldsymbol{x} = \sum_{a=1}^{8} N_a(\xi_1, \xi_2, \xi_3)\boldsymbol{x}_a. \tag{2}$$

Using elements in initial configurations [such as those presented in Fig. 1(b)] as building blocks, any geometry can be constructed.

The deformation gradient $\hat{\boldsymbol{F}} = \partial \boldsymbol{x}/\partial \boldsymbol{X}$, which describes the deformation, can be derived using (1) and (2), and has the following form:

$$\hat{\boldsymbol{F}} = \frac{\partial \boldsymbol{x}}{\partial \boldsymbol{X}} = \sum_{a=1}^{8} \boldsymbol{x}_a \otimes \frac{\partial N_a}{\partial \boldsymbol{X}} \tag{3}$$

where $\otimes$ is a symbol of a tensor product of two vectors. The result of a tensor product of two vectors is a matrix (second-order tensor). $\partial N_a/\partial \boldsymbol{X}$ can be expressed in the variables of the local coordinate system using the chain rule as follows:

$$\frac{\partial N_a}{\partial \boldsymbol{X}} = \left(\frac{\partial \boldsymbol{X}}{\partial \boldsymbol{\xi}}\right)^{-T} \cdot \frac{\partial N_a}{\partial \boldsymbol{\xi}} \tag{4}$$

where $-T$ denotes transpose inverse. In order to make the calculation more convenient, we evaluate the deformation gradient only for eight points inside each element. These points are referred to as *Gauss points* since the coordinates of these points are determined the same way as positions of abscissas in the *Gaussian quadratures* method [7]. Because of that, the $\partial N_a/\partial \boldsymbol{\xi}$ is precalculated only for eight Gauss points inside the element and stored. It follows that

$$\partial \boldsymbol{X}/\partial \boldsymbol{\xi} = \sum_{a=1}^{8} \boldsymbol{X}_a \otimes \partial N_a/\partial \boldsymbol{\xi}$$

for the given initial configuration is also precalculated and stored for each element.

If the direction of the fibers in an initial configuration is known and is represented by the unit vector $\boldsymbol{L}$, a new unit vector of the fiber direction $\boldsymbol{l}$ and the fiber extension ratio λ in the deformed configuration are given by the following:

$$\lambda \boldsymbol{l} = \hat{\boldsymbol{F}}\boldsymbol{L}. \tag{5}$$

In the computer implementation, since the deformation gradient is calculated only for Gauss points in each element, the directions of fibers, $\boldsymbol{L}$, only need to be known at these points.

To model the incompressibility during a deformation, the Jacobian of the deformation gradient, $J = \det \hat{\boldsymbol{F}}$ is constrained to a value of 1 for each of the Gauss points.

B. Deformation Driving Forces

In this study the model was deformed two ways. One deformation was driven by minimizing an objective function based on fiber shortening characteristics. The other deformation was driven by minimizing a cost function based on image-driven components. These two types of deformation are referred to as *fiber driven* deformation and *image driven* deformation, and the cost functions are denoted as f_λ and f_I, respectively.

The fiber driven objective function has the following form:

$$f_\lambda(x_1, \ldots, x_N) = \sum_{e=1}^{M}\sum_{g=1}^{8} \times \left\{(\lambda_{eg}(x_1, \ldots, x_N) - \hat{\lambda}_e)^2 + \alpha(J_{eg} - 1)^2\right\} \tag{6}$$

where $x_1, \ldots, x_N$ are the positions of the nodes and N is the number of nodes in the model. The value of the fiber extension for each Gauss point g in element e for the current configuration of nodes $x_1, \ldots, x_N$ was given by $\lambda_{eg}(x_1, \ldots, x_N)$. The desired extension for element e was given by $\hat{\lambda}_e$. The term $\alpha \cdot (J_{eg} - 1)^2$ ensured incompressibility where J_{eg} was the value of the Jacobian for Gauss point g in element e, and α was a penalty constant.

The image driven deformation was based on minimizing the difference between two cardiac images. Taking two different images of the heart at different time gates, one image becomes a source S, from which the deformation will begin and the other image is a target T. Because the images are voxel based, in order to use our parametric model a transformation that will create the mesh of the deformable model from the source image is needed. In this paper we assume that an appropriate finite element mesh has already been fitted to the image data. The creation of meshes for each gate using gated SPECT data was investigated in [8].

In order to drive the model from the source configuration to the target configuration each node has been assigned intensity I_n^S using the source image. As mentioned in the introduction, since nodes are "attached" to the material, the intensity of the nodes should remain the same during deformation. As a result, the target configuration intensity of the nodes that correspond to the target image I_n^T should be the same as I_n^S. Therefore, the objective function f_I is defined as follows:

$$f_I(x_1, \ldots, x_N) = \sum_{n=1}^{N} \left[I_n^T(x_n) - I_n^S\right]^2 + \sum_{e=1}^{M}\sum_{g=1}^{8}\Big\{\alpha \cdot (J_{eg} - 1)^2 + \beta \cdot \left[\lambda_{eg}(x_1, \ldots, x_N) - \bar{\lambda}(x_1, \ldots, x_N)\right]^2\Big\} \tag{7}$$

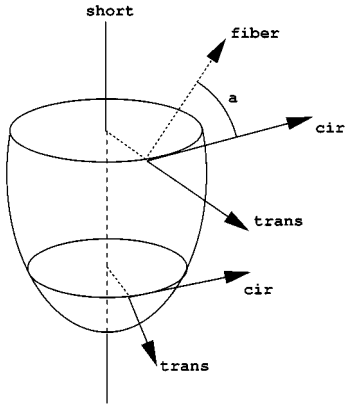

Fig. 2. Diagram representing directions in a heart model. The "cir" and "trans" stand for circumferential and transmural directions. The transmural direction is perpendicular to the surface, and the circumferential direction is parallel to the surface and perpendicular to the long axis. The angle a is the angle between the fiber direction "fiber" and the circumferential direction. Fiber direction is also perpendicular to the transmural direction.

with $\bar{\lambda}$ being an average λ over the object defined as

$$\bar{\lambda}(x_1,\ldots,x_N)=\sum_{e=1}^{M}\sum_{g=1}^{8}\frac{\lambda_{eg}(x_1,\ldots,x_N)}{8N}. \tag{8}$$

The value of $I_n^T(x_n)$ is mapped using tri-quadratic interpolation. That is, the value of $I_n^T(x_n)$ was a weighted average of 27 pixels surrounding the coordinate x_n. The weights used were appropriate to quadratic interpolation. Quadratic interpolation was used to preserve the continuity of the derivative of f_I.

In (7), there was an additional regularization term with a penalty constant β. It is assumed that there was little variability in the extension ratios throughout the heart muscle. Without this regularization, the fiber extension for some fibers would have been much higher than for others. For real cardiac tissue this is not the case since the activation of the heart muscle is relatively uniform throughout the heart muscle volume.

Both objective functions f_λ and f_I were minimized using the standard conjugate gradient method [7]. Gradients were calculated numerically using double float precision.

III. Results

We tested our model using a simple cylindrical geometry. The cylinder was a good approximation of the equatorial region of the heart [9]. The fiber orientation in the simulation of the cylinder varied linearly from a -60° angle with circumferential direction for the epicardial wall to 60° for the endocardial wall. The circumferential direction was in the plane perpendicular to the surface of the object and was also perpendicular to the short axis of the heart. All directions, and the fiber angle, are schematically shown in Fig. 2.

The radii of the cylinder were 1 and 2 cm and the cylinder was 2 cm long [Fig. 3(a)]. The cylinder consisted of 480 nodes and 320 elements. Using (6), the cylinder was contracted to a configuration in which the fiber extension ratios were equal to $\lambda = 0.85$. The result is presented in Fig. 3(b).

Contraction of an abnormal heart was also simulated using (6). For this simulation, one angular section was "dead" and the assumed λ for that section equaled 1. Two neighboring sections

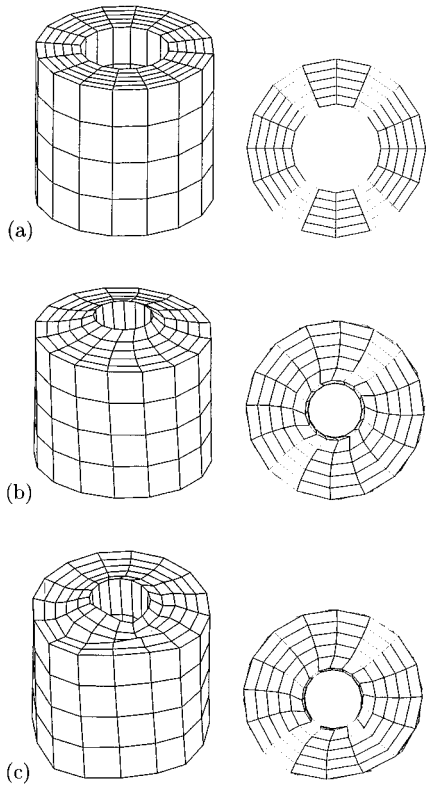

Fig. 3. Kinematic simulation of the cylinder. The left column is a three-dimensional (3-D) view, and the right column is a view from the top. (a) The first row is a cylinder in initial configuration. (b) The second row after a contraction to $\lambda = 0.85$. (c) The third row shows the contracted cylinder with the dead sector located in the lower right part of the top view (at 5 o'clock).

were forced to contract to $\lambda = 0.95$, and the rest of the model to $\lambda = 0.85$. The result of this simulation is presented in Fig. 3(c).

Computer generated analytic images with cylindrical symmetry presented in Fig. 4 were used as source and target images to drive the deformation. The intensity of the images had a Gaussian profile through the heart wall. The width at half of the maximum was 1 cm for the diastole image and 1.3 cm for the systole image [Fig. 4(a) and (b)]. Uneven thickening was simulated by setting the width at half maximum to 1.1 cm and 1.5 cm for the lower and upper parts of the heart, respectively [Fig. 4(c)].

The deformable model of the cylinder described earlier was deformed from a diastole to a systole configuration using (7). Two simulations were performed in which the systole configuration with even (Fig. 4(b)) and uneven (Fig. 4(c)) thickening around the heart wall were used.

An ellipsoidal model of the left ventricle was also simulated. Similar to the cylindrical model, the fiber orientation varied linearly from the epicardial to the endocardial wall. The angle of the fiber direction with circumferential direction was -60° for the epicardial wall and 60° for the endocardial wall. The direction of fibers was also perpendicular to the transmural direction (Fig. 2). The model consisted of 2160 nodes and 1680 elements. The initial (diastole) configuration is presented in Fig. 5(a).

The $128 \times 128 \times 128$ pixel images of the ellipsoidal left ventricle (LV) in systole and diastole configuration were generated and smoothed with Gaussian kernels with a width at half of the

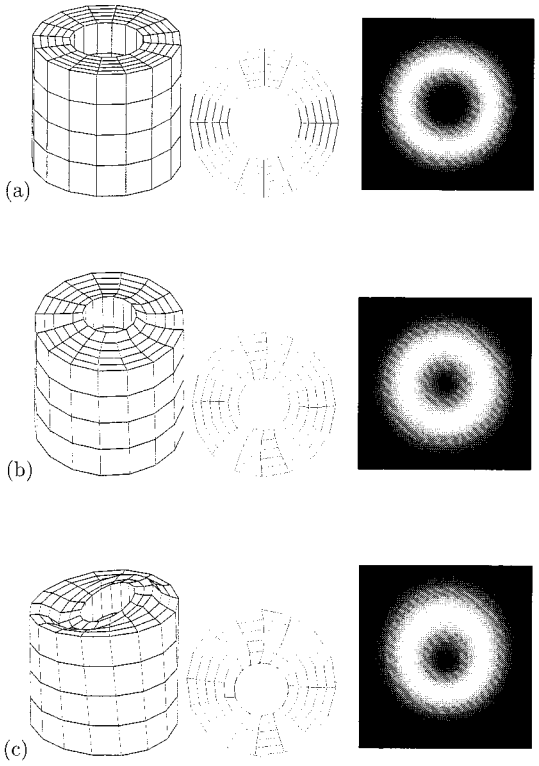

Fig. 4. Cylindrical model of the left ventricle. Each row shows 3-D and top views of the model. The images in each row were used to drive the deformation of the diastole configuration (a) to the systole configuration (b) and (c). Configuration (c) corresponds to a case of uneven thickening of the myocardium.

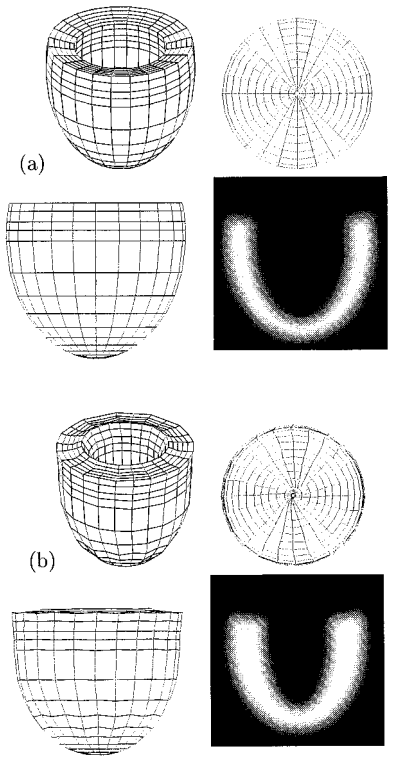

Fig. 5. Ellipsoidal model of the left ventricle (LV). The 3-D, top, and side views for simulation at diastole (a) and systole (b). The images of central long-axis views of the left ventricle, which were used to deform the model from diastole configuration to systole configuration, are also shown.

maximum equal to 3 cm. The size of the pixel was 0.0625 cm. The central long-axis views of these images are presented in Fig. 5.

These images were used to drive the deformation using (7) from the diastole configuration [Fig. 5(a)] to the target configuration [Fig. 5(b)].

IV. Discussion

As shown in Fig. 3, the heart movement during contraction is very complex. Most imaging techniques can only detect radial movement, when in fact, there is also substantial torsional movement. It can be seen that torsion in the epicardial and endocardial walls is different. During the contraction of our model, the outer radius of the heart does not change as much as the inner radius. Also, the length of the cylinder changes considerably. This finding is consistent with results of other investigators [9].

In the second example, an infarct was simulated where the heart material in one of the angular segments was not able to contract. It can be seen in Fig. 3 that the heart wall does not thicken enough in that region, and that greatly affects the ejection fraction when compared to the normal configuration.

A similar torsional movement was visible in the simulation of the heart deformation when the deformation was derived by the imaging data. The imaging data were similar to data acquired by gated SPECT or PET. So, with the help of the deformable model more features of the movement can be found from these imaging modalities.

During all simulations, it was assumed that the fiber orientations were known and that they were the same for all experiments. In reality, the fiber orientation is not necessarily the same for each heart. The very interesting problem of the impact of fiber orientation distributions on heart movement can be investigated using the deformable model with fiber structure.

The validation of the model presented in this paper is very important. The value of the constant β in (7) can slightly change the final deformed configuration, so the most appropriate β for human heart muscle has to be determined. We plan to use a tagged MRI technique that can determine the whole deformation tensor of the heart movement to validate our model and to determine parameters α and β that are best suited for the human heart.

Ultimately, we plan to use this deformable model to simulate LV or even the whole heart movement during the contractions. The impact of infarcts on this movement, and on diagnostically important LVEF or heart thickening can be studied and parameterized. Also, using this model and imaging data *a priori*, more precise LVEF and wall thickening can be found than from nuclear medicine studies alone.

References

[1] G. J. Klein, "Forward deformation of PET volumes using nonuniform elastic material constraints," *Inform. Processing Med. Imaging*, vol. 1613, pp. 358–363, 1999.

[2] J. M. Huyghe, T. Arts, D. H. van Campen, and R. S. Reneman, "Porus medium finite element model of the beating left ventricle," *Amer. J. Physiol.*, vol. 262, pp. H1256–H1267, 1992.
[3] R. D. Rabbitt, J. A. Weiss, G. E. Christiansen, and M. I. Miller, "Mapping of hyperelastic deformable templates using the finite element method," *Proc. SPIE V*, vol. 2573, pp. 252–265, 1995.
[4] J. Bonet and R. D. Wood, *Non-Linear Continuum Mechanics for Finite Element Analysis*. Cambridge, U.K.: Cambridge Univ. Press, 1997.
[5] A. Sitek, E. V. R. Di Bella, and G. T. Gullberg, "Use of imaging data in modeling of heart deformation by finite element methods," in *IEEE Nuclear Science Symp. and Medical Imaging Conf. Rec.*, Seattle, WA, Oct. 24–30, 1999, pp. 1566–1568.
[6] J. D. Humphrey and F. C. P. Yin, "On constitutive relations and finite deformations of passive cardiac tissue: I. A pseudostrain-energy function," *J. Biomech. Eng.*, vol. 109, pp. 298–304, 1987.
[7] W. H. Press, S. A. Teukolsky, W. T. Vetterling, and B. P. Flannery, *Numerical Recipes in C*. Cambridge, U.K.: Cambridge Univ. Press, 1996.
[8] B. Feng, A. Sitek, and G. T. Gullberg, "The prolate spheroidal transformation for gated SPECT," *IEEE Trans. Nucl. Sci.*, vol. 48, pp. 872–875, June 2001.
[9] J. M. Guccione, A. D. McCulloch, and L. K. Waldman, "Passive material properties of intact ventricular myocardium determined from a cylindrical model," *J. Biomech. Eng.*, vol. 113, pp. 42–55, 1991.